Steering hydrocarbon selectivity in CO_2 electroreduction over soft-landed CuO_x nanoparticle-functionalized gas diffusion electrodes

Reference:
Daems Nick, Choukroun Daniel, Merino Pablo, Rettenmaier Clara, Pacquets Lien, Bergmann Arno, Santoro Gonzalo, Vazquez Luis, Martinez Lidia, Cuenya Beatriz Roldan, ...- Steering hydrocarbon selectivity in CO_2 electroreduction over soft-landed CuO_x nanoparticle-functionalized gas diffusion electrodes
ACS applied materials and interfaces - ISSN 1944-8252 - Washington, Amer chemical soc, 14:2(2022), p. 2691-2702
Full text (Publisher's DOI): https://doi.org/10.1021/ACSAMI.1C17998
To cite this reference: https://hdl.handle.net/10067/1854910151162165141

Steering Hydrocarbon Selectivity in CO_2 Electroreduction over Soft-Landed CuO_x Nanoparticle-Functionalized Gas Diffusion Electrodes

Nick Daems,[a,*,‡] *Daniel Choukroun,*[a,‡] *Pablo Merino,*[b] *Clara Rettenmaier,*[c] *Lien Pacquets,* [a,d] *Arno Bergmann,*[c] *Gonzalo Santoro,*[b] *Luis Vázquez,*[b] *Lidia Martínez,*[b] *Beatriz Roldan Cuenya,*[c] *Jose Angel Martín Gago,*[b] *Tom Breugelmans*[a,*]

[a] Applied Electrochemistry and Catalysis (ELCAT), University of Antwerp, 2610 Wilrijk, Belgium

[b] ESISNA research group, Institute of Materials Science of Madrid (CSIC), 28049 Madrid, Spain

[c] Department of Interface Science, Fritz-Haber Institute of the Max-Planck Society, 14195 Berlin, Germany

[d] Electron Microscopy for Materials Science (EMAT), University of Antwerp, 2020 Antwerp, Belgium

KEYWORDS: copper, nanoparticles, gas diffusion electrodes, CO_2 electroreduction, sputter gas aggregation source

ABSTRACT

The use of physical vapor deposition methods in the fabrication of catalyst layers holds promise for enhancing the efficiency of future carbon capture and utilization (CCU) processes such as the CO_2 reduction reaction (CO_2RR). Following that line of research, we report in this work the application of a sputter gas aggregation source (SGAS, multiple ion cluster source (MICS) type) apparatus, for the controlled synthesis of CuO_x nanoparticles (NP) atop gas diffusion electrodes. By varying the mass loading, we achieve control over the balance between methanation and multicarbon formation in a gas-fed CO_2 electrolyzer, and obtain peak CH_4 partial current densities of -143 mA cm^{-2} (mass activity 7.2 kA/g) with a Faradaic efficiency (FE) of 48%, and multicarbon partial current densities of -231 mA cm^{-2} at 76% FE (FE_{C2H4} = 56%). Using Atomic force microscopy, electron microscopy and *quasi in-situ* X-ray photoelectron spectroscopy, we trace back the divergence in hydrocarbon selectivity to differences in NP film morphology, and rule out the influence of both NP size (3-15 nm, > 20 µg cm^{-2}) and *in-situ* oxidation state. We show that the combination of O_2 flow rate to the aggregation zone during NP growth and deposition time, which affect the NP production rate and mass loading, respectively, give rise to the formation of either densely packed CuO_x NPs or rough three-dimensional networks made from CuO_x NP building blocks, that in turn affect the governing CO_2RR mechanism. This study highlights the potential held by SGAS-generated NP films for future CO_2RR catalyst layer optimization and upscaling, where the NPs' tunable properties, homogeneity and the complete absence of organic capping agents may prove invaluable.

INTRODUCTION

The CO_2 Reduction Reaction (CO_2RR) - powered by electricity from renewable energy – could offer a route for generating value-added chemicals from residual CO_2 emissions, and would potentially bring us a step forward towards closing the anthropogenic carbon cycle.[1-3] Myriad studies have demonstrated that copper has the unique ability to reduce carbon dioxide to hydrocarbons and alcohols, with recent endeavors using evaporated copper films reporting high methane and ethylene selectivities with promising energy efficiency and longevity.[4-7]

In the cases where catalyst layers were made up of copper (oxide) nanoparticle (NP) assemblies, the NP size,[8] faceting,[9-12] surface roughness[13] and interparticle distance[14-15] have been shown to impact the CO_2RR performance and the balance between ethylene and methane formation. Several studies demonstrated that by minimizing the distance between adjacent Cu nanoparticles, it is possible to improve CO re-adsorption on neighboring Cu sites, thereby increasing the CO coverage and thus C-C coupling efficiency towards C_{2+} products.[9, 15-16] A recent study also highlighted the importance of catalyst layer thickness at the triple-phase-boundary, as thicker layers result in decreasing local CO_2 and increasing local CO partial pressures relative to the gas flow field, both being beneficial for C-C coupling.[17] Moreover, in the particular case of either thermally or electrochemically grown copper oxide films, the role of surface morphology/roughness, subsurface oxygen and processing conditions have also been cited as important factors that govern CH_4 versus C_2H_4 production.[18-21]

Those studies have shown the importance of having proper control over NP generation and catalyst layer properties as even small modifications can result in drastic changes in CO_2RR performance. For this reason, an alternative synthesis method is investigated in this work, which allows to deposit CuO_x nanoparticles directly onto gas diffusion electrodes (GDEs) while providing control over their initial oxidation state and mass loading. Building on the advantages of conventional physical vapor deposition methods already used in the CO_2RR literature,[22-24] this physical deposition method includes a state-of-the-art sputter gas aggregation source (SGAS, multiple ion cluster source (MICS) type) and a specifically tailored aggregation zone. Moreover, this technique offers a fast, reproducible and tunable approach to deliver nanoparticles of various metals and oxidation states.[25-27] An important advantage of this technique[28] over wet chemical synthesis methods is that neither organic ligands nor ion-exchange polymers are present during the synthesis of those nanoparticles or during catalyst ink preparation, which could otherwise influence what we perceive as the intrinsic catalytic activity of the particles.

Here, we used the capabilities of the MICS to fabricate CuO_x nanoparticle films with varying mass loadings and primary particle size below 15 nm, and investigated their CO_2RR performance under various processing conditions. We started by examining the visual and microscopic properties of the NP films, as well as their oxidation state after preparation, storage and polarization at various potentials. After presenting our findings, we report on how those properties dictate the electrodes' surface area and electrochemical activity, both in an H-type cell as in a flow cell configuration. By employing the latter, we show that Cu_2O NP-functionalized (NPF) electrodes fabricated by means of a MICS are capable of producing in 1M $KHCO_3$ either methane or C_{2+} products with high mass-based activities and selectivities. Finally, the prospects of SGAS fabrication for the optimization of CO_2RR catalyst layers are briefly put forward.

METHODS

Nanoparticle synthesis and deposition

CuOx (x = 0-1) nanoparticles were produced in the STARDUST machine[26] (see Figure S1) under ultra-high vacuum conditions (base pressure 5 x 10^{-10} mbar) using a Multiple Ion Cluster Source (MICS3, Oxford Applied Research Ltd., UK), details of which are given elsewhere.[27, 29]

For the electrocatalysts synthesized and utilized in this work, we used one of the three magnetrons sources available, which was loaded with a copper target (99.99% pure, 4 mm thick and 2" diameter, Testbourne Ltd., UK). To control the oxidation state of the nanoparticles during formation, oxygen injection in the aggregation zone was adjusted from 0 sccm to 0.8 sccm to 21.3 sccm, to predominantly produce Cu, Cu_2O and CuO nanoparticles, respectively. Once produced at the source, CuO_x nanoparticles were collected on Si(100) wafers for AFM measurements and Sigracet 39 BC (SGL Carbon) gas diffusion electrodes (GDEs) for electrochemical analysis. The deposition rate was determined with a quartz microbalance and the coverage was controlled by modifying the deposition time. NP-functionalized (NPF) Electrodes are referred to in the main text as **Cu_{NPF}**, **Cu_2O_{NPF}** and **CuO_{NPF}**, after their predominant oxidation state as prepared. Where needed, the mass loading (expressed in µg cm^{-2}) is given in parentheses, as in **Cu_2O_{NPF}(20)**. All the samples are listed and indexed according to their appearance in the text in Table S1.

Characterization

X-ray Photoelectron Spectroscopy

Initial and after reaction *ex situ* XPS measurements were performed in the analysis module of the STARDUST machine[26] utilizing a PHOIBOS 100 1D electron/ion analyzer with a monochromatic Al Kα anode (1486.6 eV) and a 1D delay line detector. CuO_x nanoparticles were deposited onto the GDE, which was inserted in the analysis chamber and analyzed with XPS. The Cu 2p, O 1s core levels and

Cu_{LMM} Auger lines were recorded and the binding energies were corrected with respect to the C 1s core level peak (284.5 eV).

In addition, quasi *in situ* XPS measurements were conducted in a different UHV system with a commercial PHOIBOS 100 analyzer (SPECS GmbH, E_{pass} = 15 eV) and a XR50 X-ray source (SPECS GmbH) using an Al Kα anode (1486.6 eV) anode. The accompanying electrochemical measurements were performed with a potentiostat (Autolab PGSTAT 302N) in an air-tight single compartment cell with a leak free Ag/AgCl reference electrode (eDaq 1mm, 3.4M KCl) and a platinum gauze electrode (MaTecK, 360 mesh cm^{-2}) as counter electrode under constant CO_2 bubbling in purified 0.1M $KHCO_3$. The electrochemical cell is directly attached to the UHV analysis system. After the electrochemical treatment, the samples were washed with Ar-saturated water (≥18 MΩ) and then transferred within a controlled N_2 atmosphere into the UHV system without air exposure.

Atomic Force Microscopy

In order to determine the NP morphology *ex-situ*, Atomic Force Microscopy (AFM) images were recorded on flat Si(100) wafers instead of on the GDEs. The GDEs have a very high surface roughness and therefore do not allow correct characterization of the height (and thus diameter[30]) of the nanoparticles. AFM measurements were performed using a Cervantes AFM System equipped with the Dulcinea electronics from Nanotec Electronica S.L. and a Nanoscope IIIa system (Veeco) and Agilent 5500 PicoPlus (Agilent). All images were analyzed using WSxM software.[31]

Scanning Electron Microscopy

Scanning electron microscopy (SEM) images were taken using a ThermoFisher Scientific Quanta FEG 250 microscope, equipped with ETD and Quad BSED detectors, and operated at an acceleration voltage of 15 kV.

Inductively Coupled Plasma Mass Spectrometry

The Cu mass loadings of the films were quantified using an Agilent 7500 Series Inductively Coupled Plasma Mass Spectrometer (ICP-MS). Disks of coated GDEs taken from fresh and aged electrodes were subjected to digestion in nitric acid at 70°C overnight. The solutions were then diluted to the appropriate concentration range (100-300 ppb) prior to analysis.

Contact angle measurements

Sessile drop measurements were carried out using a Drop Shape Analyzer (DSA) 10-Mk2 device (Krüss GmbH) by drop-casting 2 µL of ultrapure water at a rate of 24.79 µL min^{-1} onto the coated side of the GDE surface at room temperature. The surfaces were imaged at a rate of 1 Hz for 1 min and analyzed with the DSA software. The average values of the contact angle measurements are reported.

Electrochemistry

Chronopotentiometry/Flow Cell Experiments

Chronopotentiometry was conducted using an Autolab M204 potentiostat/galvanostat in a flow by gas-fed recycle electrolyzer configuration, in which the catholyte (either 0.1 M or 1 M $KHCO_3$) was continuously recycled throughout the experiment (total volume 4-5 cm³). The working electrode consisted of a CuO_x-sputtered gas diffusion electrode (Sigracet 39 BC) with an active area of 0.785 cm^2. A leak-tight 1 mm Ag/AgCl was used to monitor the working electrode potential (3M KCl, +0.210 V vs. SHE, Harvard Apparatus), which was corrected for ohmic drop (IR_u) and electrolyte pH according to (Eq. 1):

$$E\ (\text{V vs. RHE}) = E\ (\text{V vs. Ag/AgCl}) - I{*}R_u + 0.059{*}\text{pH} + 0.21\ \text{V} \tag{1}$$

,with R_u determined by means of current interrupt (0.1 M $KHCO_3$) and electrochemical impedance spectroscopy (1 M $KHCO_3$, frequency range: 20 kHz - 5 kHz, 20 mV perturbation amplitude) experiments. Carbon cloth was used as counter electrode adjacent to a Selemion® DSVN anion-exchange membrane (AGC Chemicals Europe, Ltd.), separating the catholyte and anolyte compartments. The inlet and exiting gas streams were continuously controlled (5-7.5 sccm CO_2, 99.995%) and measured, respectively, using mass flow controllers (GF-080, Brooks Instruments). The outlet gas stream was sampled in-line at 15 min intervals by means of a gas chromatograph (GC, Trace 1300, Thermo Fischer Scientific). Products were separated using a ShinCarbon micropacked column (ST 100/120, 1 mm ID, 2 m, Restek) and detected by a thermal conductivity detector (TCD). Helium was used as the carrier gas. Liquid products (glyoxal, formic acid, ethanol, acetic acid, n-propanol and allyl alcohol) were sampled from both, catholyte and anolyte (to a lesser extent) and quantified by GC equipped with a flame ionization detector (FID) detector and high-performance liquid chromatography (HPLC, Alliance 2695, Waters). The Faradaic efficiency (FE) of the different products was calculated using following equation (Eq. 2):

$$FE_i\,(\%) = Q_{exp,i}/Q_{total} = z_iFn_i/It \tag{2}$$

, where $Q_{exp,i}$ is the amount of charge consumed for the production of product i, Q_{total} is the total accumulated charge, F the Faraday constant (F, 96485 C mol^{-1}), z_i the number of exchanged electrons for each specific product and n_i the number of moles of product (n_i). Q_{total} is the product of applied current (I) and experiment duration (t).

Chronoamperometry/H-type cell Experiments

Chronoamperometry experiments were performed with a potentiostat (Autolab PGSTAT 302N) in an H-type cell equipped with an anion exchange membrane (Selemion® AMV) which separates the cathodic from the anodic compartment. The anodic compartment was equipped with a platinum gauze electrode (MaTecK, 360 mesh cm^{-2}), while a leak-free Ag/AgCl reference electrode (eDaq 2mm, 3.4M KCl) was placed close to the GDE working electrode in the cathodic compartment. 0.1 M $KHCO_3$ (Alfa Aesar, 99.7 – 100.5%) was purified with a cation-exchange resin (Chelex 100 Resin, Bio-Rad), saturated with CO_2 (99.995%) and used as electrolyte. Prior to the 70 min chronoamperometric measurement, a linear sweep from open circuit potential to the desired potential was conducted. Every 15 min, the gas products were quantified by online ~~gas chromatography (~~GC~~,~~ (Agilent 7890B), which is provided with a flame ionization detector (FID) and a TCD. At the end of the electrochemical measurement, the liquid products were probed in a liquid GC (L-GC, Shimadzu 2010plus) with a fused silica capillary column and an FID detector, and in an HPLC (Shimadzu Prominence), provided with a refractive index detector (RID) and a NUCLEOGEL SUGAR 810 column. Double layer capacitance (C_{DL}) was measured via cyclic voltammetry between -0.25V and -0.4V vs. Ag/AgCl, with scan rates between 20 and 160 mV s^{-1}. Each sample was also measured upon CO_2RR conditioning at three different potentials.

RESULTS AND DISCUSSION

Characterization of the As-prepared Film Morphology and Oxidation States

Figure 1 gives an overview of the appearance, morphology and oxidation state of CuO_x NPs that were deposited atop the microporous layer of gas diffusion electrodes using the Stardust machine (Figure 1a). Above a mass loading threshold of about 20 µg cm^{-2}, the films are visually characterized by an iridescent pattern radiating outward from the center of the GDE substrate, as shown in Figure 1b1. That feature arises from the Gaussian particle beam shape and its divergence at the exit of the MICS module of the apparatus, which induces a radial variation in NP film thickness/areal density and catalyst layer composition as one moves away from the beam center (see Figure S2). Electrodes with mass loadings ≤ 10 μg_{Cu} cm^{-2}, however, appear as featureless black GDE substrates to the naked eye and the NP films can only be distinguished from the microporous layer background by electron microscopy. For example, Figure 1b2 shows densely packed CuO_x particle clusters atop a GDE at a mass loading of 5 µg cm^{-2}. At higher mass loadings, Figure 1b3-4 show that either porous (~10 μg_{Cu} cm^{-2}) or dense (≥20 μg_{Cu} cm^{-2}) three-dimensional film structures can be obtained from CuO_x NP building blocks. With the deposition time kept fixed, the electrodes' Cu mass loading naturally depends on the production rate of CuO_x NPs (typically 0.03-0.15 µg cm^{-2} s^{-1}), which increases substantially with the O_2 flow rate to the aggregation zone. As a direct consequence, mass loadings in the following discussion were systematically lower for CuO_x NP films that were prepared in the absence of O_2 (≤ 8 µg cm^{-2}) when compared to CuO_x NP films where the O_2 flow was set to 0.8 sccm and 21.3 sccm (≥20 µg cm^{-2}).

In Figure 1c, representative high-resolution Cu 2p spectra are shown that were taken inside the analysis section of the apparatus, that is, without exposing the NPs to air. At 21.3 sccm O_2**,** the spectrum can be partially attributed to a +II oxidation state, both from the Cu 2p peak position (932.8 eV) and the pronounced Cu 2p shake-up satellites emerging at 940.6, 943.0

and 961.7 eV. The intensity of those Cu 2p shake-up satellite peaks is lower for the NP film prepared with 0.8 sccm O_2., and the Cu $2p_{3/2}$ peak is shifted to ~931.5 eV. In the absence of an O_2 flow (0 sccm O_2), the Cu $2p_{3/2}$ peak is located at 932.5 eV and no shake-up satellites are observed. Differentiation between metallic Cu and Cu(I) for 0 and 0.8 sccm O_2 is further facilitated by analysis of the Auger Cu LMM spectra (Figure 1d).

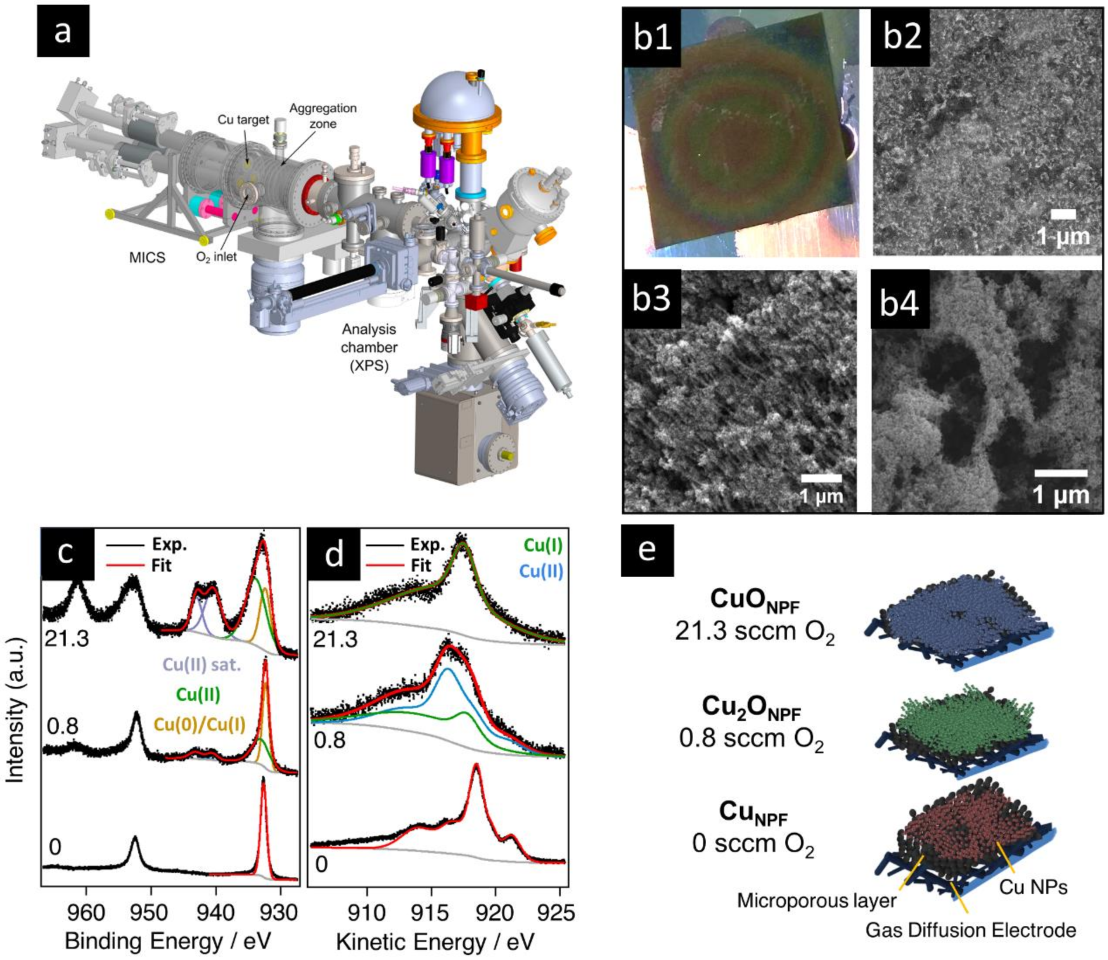

Figure 1 *(a) Illustration of the Cu nanoparticle generator, MICS and analysis section. (b1) Photograph of a CuO_x NP film deposited onto a gas diffusion electrode (b2) Backscattered electron SEM image of CuO_x NP clusters, film mass loading ~5 µg cm^{-2}, O_2 flow rate: 0 sccm. (b3) SEM image of CuO_x NPs showing aggregates, film mass loading ~10 µg cm^{-2}, O_2 flow rate: 0.8 sccm. (b4) SEM image of a dense CuO_x -NP film, film mass loading ~20µg cm^{-2}, O_2 flow rate: 21.3 sccm. XPS analysis inside the analysis section: (c) Cu 2p and (d) Auger Cu_{LMM} spectra of NP-films prepared with varying O_2 flow rates: 0, 0.8 and 21.3 sccm O_2, respectively, yielding (e)* ***Cu_{NPF}*** *,* ***Cu_2O_{NPF}*** *and* ***CuO_{NPF}*** *electrodes.*

At 0 sccm O_2, the spectrum indicates that only metallic Cu is present. However, for 0.8 sccm and 21.3 sccm O_2, linear combination fitting (LCF) indicates that the NPs consist of 63% Cu(I)/37% Cu(II) and 100% Cu(II), respectively. Hence, for simplicity, NP-functionalized electrodes (NPF) prepared under similar O_2 flow rate conditions with 0, 0.8 sccm and 21.3

sccm O_2 are denoted in this paper as **Cu_{NPF}**, **Cu_2O_{NPF}** and **CuO_{NPF}**, respectively, according to the predominant Cu oxidation state (Figure 1e).

In addition, the presence of surface Cu(I) species in **Cu_2O_{NPF}** electrodes was also probed qualitatively using linear sweep voltammetry (LSV) in an aqueous, CO_2-saturated 0.5 M bicarbonate solution. Figure S3 shows that **Cu_2O_{NPF}** films with varying mass loadings exhibit reduction peaks characteristic of Cu(I) at 0 V and -0.4 V *vs.* RHE[32-33] that appear before the onset of the hydrogen evolution reaction (HER) and CO_2RR at more negative electrode potentials.

Combined Spectroscopic-Electrochemical Investigation of the Film behavior during CO_2RR

Next, we evaluated whether the oxidation state of films fabricated under different O_2 flow rates has a significant impact on the electrodes' electrochemical performance towards CO_2RR. Therefore, CuO_x NP-based electrodes (batches 1-3, Table S1) were probed before and directly after CO_2RR electrolysis in an H-type cell.

After prolonged storage in air and prior to electrolysis, **Cu_{NPF}** and **Cu_2O_{NPF}** electrodes showed clear signs of oxidation in their Cu 2p spectra (Figure 2a), *i.e.* more pronounced Cu(II) satellite features and a large fraction assigned to Cu(II) species. Deconvolution of the Cu LMM spectral line-shapes by LCF further indicated that 60-80% of all surfaces were completely oxidized to Cu(II), while the remaining part was attributed almost exclusively to Cu(I) (see Figure S4a and Table S2).

After 1 h of CO_2RR in 0.1M $KHCO_3$ (pH 6.8) at -0.85V vs. RHE (V_{RHE}), and by carefully excluding re-oxidation due to air (*quasi in situ* XPS conditions, electrochemical cell directly interfaced to the XPS UHV system), we observed that the Cu(II) satellite features disappeared completely from the Cu 2p spectra (Figure 2b). Auger Cu LMM spectra (Figure 2c) indicated, in all cases, that the surfaces were reduced almost entirely to Cu(0). Using LCF, the remaining share of Cu(I) was estimated at a mere 10%. That share was further reduced to nearly zero at -1.05 V$_{RHE}$ (Figure S4b-c and Table S2), from which we establish that Cu(0) was the predominant active phase for CO_2 reduction near and beyond that potential, corroborating recent literature.[34]

The CO_2RR selectivity of **Cu$_{NPF}$**, **CuO$_{NPF}$** and **Cu$_2$O$_{NPF}$** electrodes at these potentials is given in Figure 2d. For **CuO$_{NPF}$** and **Cu$_2$O$_{NPF}$** electrodes, the selectivity towards the major CO_2 reduction products ethylene, methane and ethanol rose as a function of potential at the expense of carbon monoxide, which in its adsorbed form *CO, is an important intermediate in their production. Namely, *CO can either undergo protonation to *CHO, yielding eventually methane, or C-C coupling (dimerization-step) with an additional *CO adsorbate - leading mainly to ethylene.[35] At the same time, the selectivity towards formate and hydrogen, which are in this case undesired by-products, decreased with electrode potential, also in general agreement with the literature on metallic copper surfaces.[36-37] In contrast, the major products observed over **Cu$_{NPF}$** up to -1.2V$_{RHE}$ were carbon monoxide (45-53%) and hydrogen (34-38%). At potentials exceeding -1.35V$_{RHE}$ the majority of carbon monoxide was converted to methane, whose selectivity peaked at 50%. The corresponding CH_4/C_2H_4 Faradaic Efficiency (FE) ratio was 12.2, whereas it was only 0.4 and 0.76 over **Cu$_2$O$_{NPF}$** and **CuO$_{NPF}$**.

As mentioned, the mass loading of **Cu$_{NPF}$** electrodes was systematically lower than that of **Cu$_2$O$_{NPF}$** and **CuO$_{NPF}$** because of the lower O_2 flow rate to the aggregation zone during synthesis (and thus NPs rate). That difference seemed to manifest itself in the electrodes' electrochemical activity and the CO_2RR reaction mechanism. Indeed, Wang *et al*[16] previously showed that NP mass loading and the areal NP density were closely correlated to the CH_4/C_2H_4 production rate and FE ratios. It was reasoned that $CO_{(g)}$ re-adsorption over surfaces with higher mass loading, areal NP density and hence shorter mean interparticle distances[14] favors

*CO dimerization and ethylene formation over methane. In addition, variation of the pH at the electrode-electrolyte interface (local pH) may also originate from differences in electrode morphology and roughness.[20] In general, the OH^- ions produced during CO_2 reduction and hydrogen evolution reactions lead to an increase in local pH relative to the bulk (well-mixed region) of the electrolyte. The magnitude of the deviation depends largely on the reaction rate (geometric current density) and bicarbonate concentration (buffer capacity).[38-41] But, since both the electrolyte concentration and the cell configuration were identical for the three catalysts,

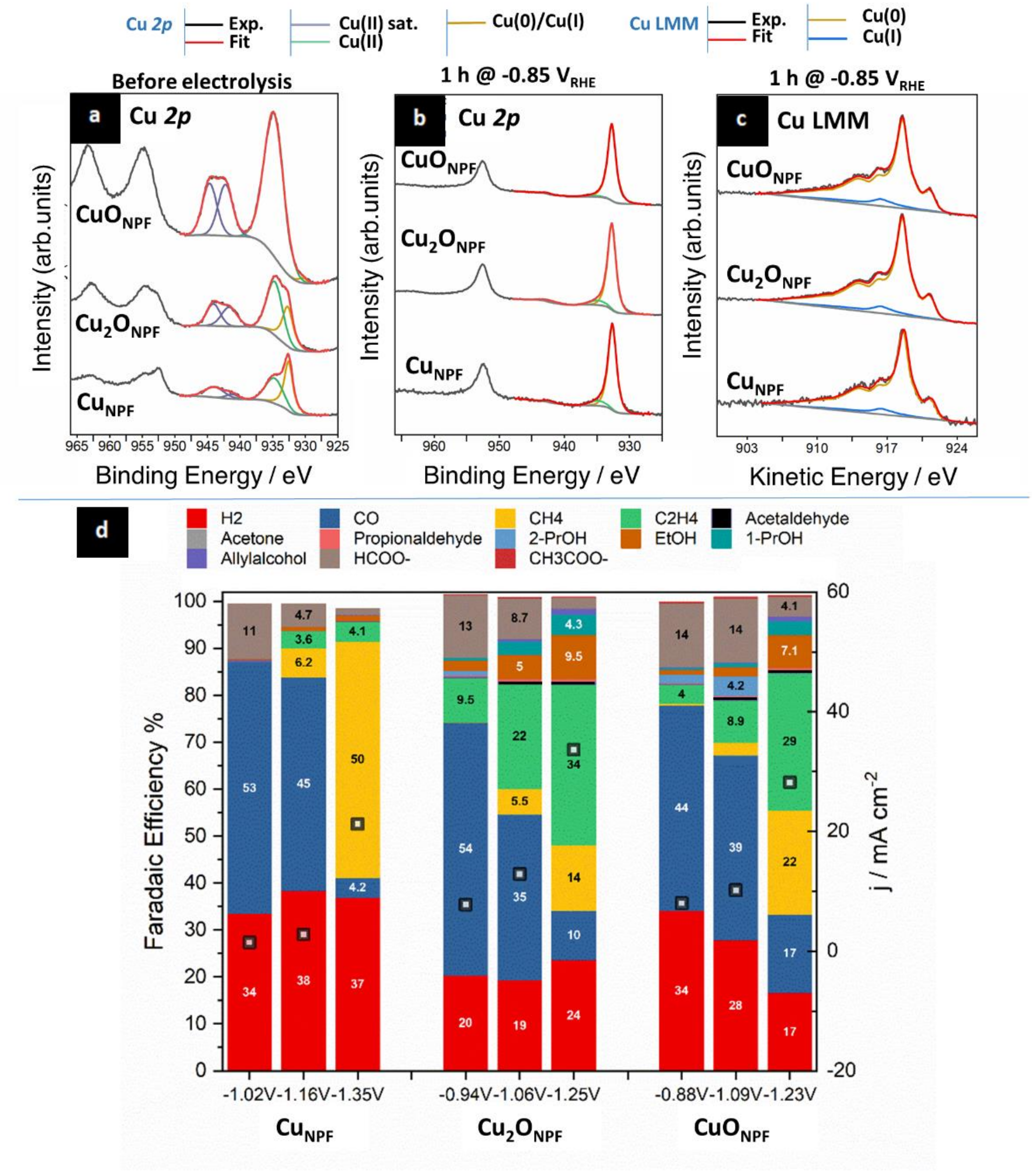

*Figure 2 (a) Cu 2p spectra of **Cu_{NPF}**, **Cu_2O_{NPF}** and **CuO_{NPF}** electrodes taken after prolonged storage in air and before electrolysis. (b) Quasi* in situ *Cu 2p spectra of the same **Cu_{NPF}**, **Cu_2O_{NPF}** and **CuO_{NPF}** taken after 1 hr of polarization at -0.85V_{RHE} in 0.1 M $KHCO_3$, (c) corresponding Cu LMM spectra and (d) H-type cell selectivity of **Cu_{NPF}**,**Cu_2O_{NPF}** and **CuO_{NPF}** electrodes as a function of the electrode potential in 0.1M $KHCO_3$.*

we reasoned that differences in local pH, if any, must stem from the electrode's morphology and its roughness.

To that end, and in order to estimate the differences in surface area between the NPF electrodes before and during CO_2RR, we performed cyclic voltammetry (CV) in a suitable potential range and analyzed the double layer capacitance (C_{DL}, expressed in µF/cm^2) of the electrode (Figure S5a), which is a measure for its electrochemically active surface area (ECSA). Unlike with flat solid electrodes, the C_{DL} averages the capacitive contribution of both the accessible NP surface area and the underlying microporous layer of the GDE. Nevertheless, we defined a roughness factor (RF) by normalization of the C_{DL} value relative to a planar electropolished Cu electrode (C_{DL} = 26.5 µF/cm^2).[34] Figure S5b shows that the RF values after polarization between -0.85 and -1.05 V_{RHE} were in the range of 15-30, with **Cu_{NPF}** having the highest RF. After polarization between -1.23 and -1.35 V_{RHE}, however, the RF increased further to 95, 49 and 59 for **Cu_{NPF}**, **Cu_2O_{NPF}** and **CuO_{NPF}**, respectively. For **CuO_{NPF}**, the RF was only 20% higher compared to **Cu_2O_{NPF}**. We therefore concluded that the general agreement between the CO_2RR selectivity trends and CH_4/C_2H_4 ratio (< 1) over **Cu_2O_{NPF}** and **CuO_{NPF}** electrodes at high overpotentials was due to the convergence in their oxidation state and roughness after polarization. When compared to both**,** the evolution of RF values in the case of **Cu_{NPF}** followed the same increasing trend but reached values about 60-90% higher, suggesting that the electrode was rougher. Rougher electrodes have a higher real surface area; they therefore deliver higher geometric current densities, which bring about a higher local pH.[40] Under such alkaline conditions, ethylene formation is said to be favored compared to proton-electron coupled reaction steps, since the rate-determining *CO coupling step does not involve a proton transfer.[42] The combination of high methane selectivity and the aforementioned RF values for **Cu_{NPF}** thus seem to be in complete contradiction with the notion that higher roughness factors translate to higher ethylene FE. However, in contrast to flat solid electrodes, that discrepancy may be attributed to an increased capacitive contribution from the underlying porous GDE, rather than to an increase in the real surface area of Cu NP ensembles. Such an explanation appears in line with the lower geometric current densities observed over **Cu$_{NPF}$** relative to **Cu$_2$O$_{NPF}$** and **CuO$_{NPF}$**. In terms of interparticle distance, the higher RF values thus point out to greater separation between the NPs and the lower current densities suggest a decrease of local pH relative to **Cu$_2$O$_{NPF}$** and **CuO$_{NPF}$**, both known to favor methane formation over ethylene, as we also observe.[43]

Importantly, the H-cell results indicated that MICS-generated CuO$_x$ films could selectively generate CH$_4$ at low mass loadings, and that selectivity control may be achieved by simply varying the sputtering deposition time.

Flow-cell CO$_2$RR performance

By supplying CO$_2$ from the gas phase in a flow cell,[44-45] higher current densities were achieved as compared to H-type cell experiments over analogous CuO$_x$ films (batches 1-3, Table S1). Figure 3 and Table S4 display the FEs of our samples when a current density of 100 mA cm^{-2} is applied. The major CO$_2$RR products over **Cu$_2$O$_{NPF}$** and **CuO$_{NPF}$** electrodes were CO, ethylene and ethanol. The total FE towards C$_{2+}$ products amounted to about 50% and 30%, respectively. These trends in selectivity were in general agreement with H-type cell measurements, yet with the important difference that both geometric ethylene partial current densities and ethylene-to-methane ratios tripled and quadrupled, respectively. As discussed in the previous section, the higher current density applied is expected to induce higher local pH conditions that favor ethylene over methane. Despite that, **Cu$_{NPF}$** still produced more CH$_4$ (24%) than ethylene (15%), although admittedly the ratio of methane over ethylene dropped to just 1.6. This nevertheless strengthened the notion that the NP areal density and mass loading had a stronger impact on the fate of the rate-determining *CO reduction step than the processing conditions (i.e. the manner in which CO_2 was fed to the solid-electrolyte interface).

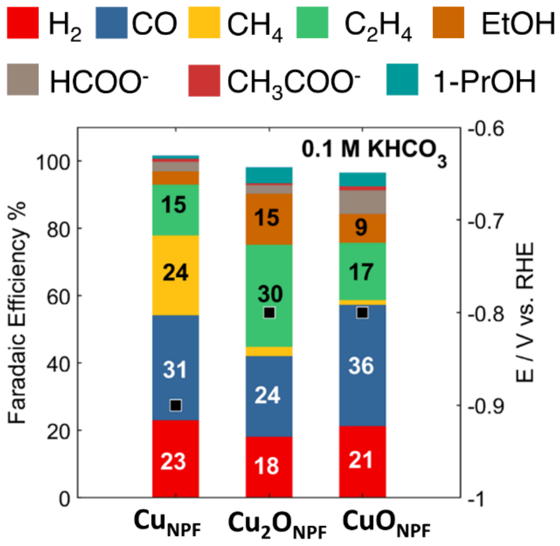

Figure 3 *Selectivity of CuO_x NP-functionalized electrodes in a gas-fed flow-cell in 0.1M $KHCO_3$ at a current density of 100 mA cm^{-2}. Black squares represent the working electrode potentials. Conditions: 5 sccm CO_2, 2 ml/min 0.1M $KHCO_3$.*

Therefore, we then proceeded to investigate the catalytic role of NP size and mass loading in more detail. A series of **Cu_2O_{NPF}** electrodes with mass loadings exceeding 20 µg cm^{-2} (batches 4-6, Tables S.1) was prepared by varying the deposition settings. For each deposition setting, CuO_x NPs were deposited both onto GDEs and for particle size determination although at much lower coverages onto Si(100) wafers. It is important to mention that size distributions representative of the NPs deposited onto GDEs could not be estimated because of the intrinsic roughness of the microporous layer of the GDE itself and because of significant particle overlap at the mass loadings studied (> 20 µg cm^{-2}). While analysis of the AFM images indicated that the nanoparticle height varied between 3 to 10 nm (Figure S6), chronopotentiometric CO_2 reduction experiments at 100 mA cm^{-2} in 0.1 M $KHCO_3$ evidenced no significant variation of the selectivity with NP size in the inspected range (Figure S7). This can be explained by the fact that the NPs reconstruct upon polarization and operation at high current densities.[43] That, in turn, may cancel out the effect of minor differences in particle size prior to polarization. As a result, the catalytic response of the formed 3D NP film resembles that of rougher and thicker oxide-derived or magnetron sputtered Cu films[46-49] rather than individual NPs or thin films in the *sub*-10 nm size range.[8, 23] Indeed, all electrodes noted C_{2+} selectivities in excess of 50% and CO_2RR selectivities surpassing 85% under the employed conditions. Hence, we concluded that **Cu_2O_{NPF}** electrodes with loadings > 20 μg cm^{-2} mainly produce ethylene and ethanol over a broad range of gas-phase synthesis parameters.

Next, to study the impact of mass loading, an additional series of **Cu_2O_{NPF}** electrodes with low mass loadings in the range of 0.1-17.8 μg cm^{-2} (batches 7-9, Table S1) was fabricated. Notwithstanding the above, the electrodes produced methane rather than ethylene as major product. Figure 4a shows LSV polarization curves, recorded in a 1M $KHCO_3$ electrolyte, of three electrodes which are denoted as **Cu_2O_{NPF}(0.1)**, **Cu_2O_{NPF} (1.8)** and **Cu_2O_{NPF} (18)**. In Figure 4b-d, partial current densities towards the major gas-phase products, namely hydrogen, carbon monoxide, methane and ethylene, are given as a function of potential. In the case of **Cu_2O_{NPF}(18)**, it can be observed that the HER clearly dominates the product spectrum up to -1.2 V_{RHE}, and it is surpassed only by methane after that point. Compared to **Cu_2O_{NPF}(1.8)**, the maximal CH_4 current density of **Cu_2O_{NPF}(18)** was 21% higher (-113.7 mA cm^{-2}) and the overpotential was lower by ~100 mV. However, the maximum methane-to-ethylene ratio over **Cu_2O_{NPF}(18)** was 3.3 and 4.2-fold lower compared to **Cu_2O_{NPF}(0.1)** and **Cu_2O_{NPF}(1.8)**, respectively, correlating with the lower overpotentials and lower activity towards hydrogen of the former. An overview of the obtained selectivities at each potential is given in Table S5.

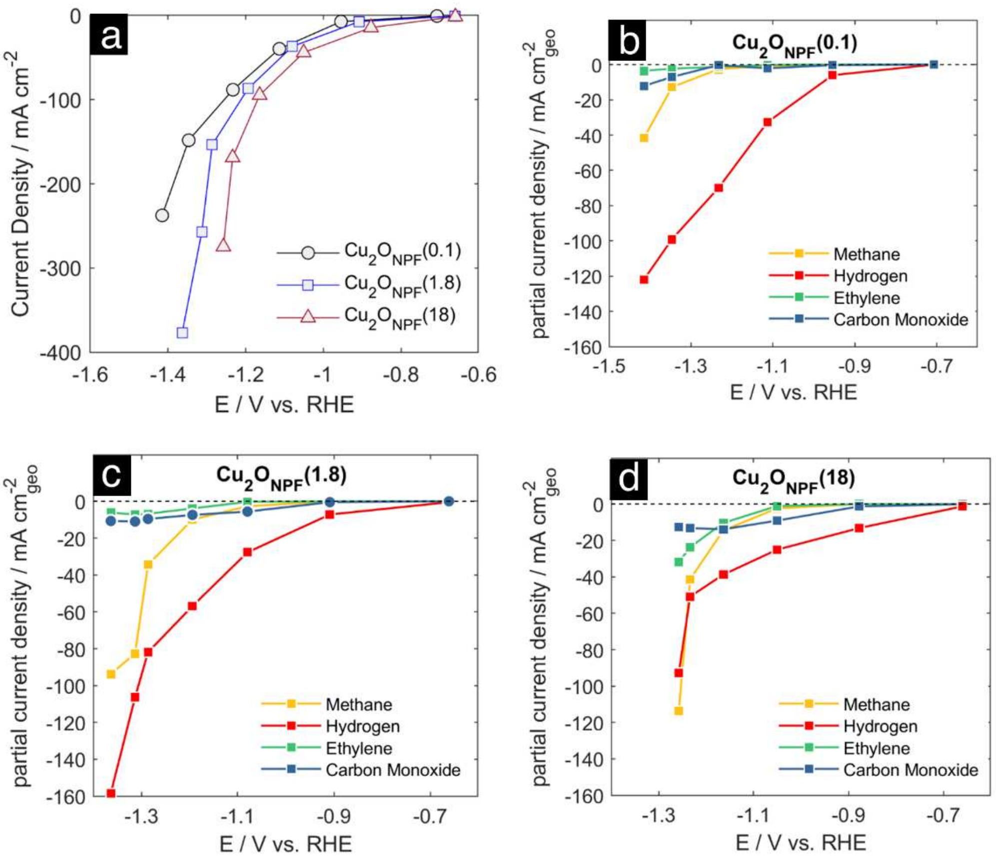

Figure 4 *(a) Total current densities as a function of potential (IR-corrected) in 1 M $KHCO_3$ for a series of* ***Cu_2O_{NPF}*** *electrodes with mass loading in the range of 0.1-17.8 μg cm^{-}.^{2} (b-d) Partial current densities towards hydrogen, carbon monoxide, methane and ethylene over* ***Cu_2O_{NPF}(0.1)***, ***Cu_2O_{NPF}(1.8)*** *and* ***Cu_2O_{NPF}(18)*** *electrodes normalized by the geometric surface area of the electrode.* *Conditions: 5-7.5 sccm CO_2, catholyte flow 0.2 ml/min, 25°C.*

Comparison of CO_2RR Performance under commercially relevant conditions

Consequently, we prepared **Cu_2O_{NPF}** electrodes with relatively low (19.8 μg cm^{-2}, **Cu_2O_{NPF}(20)**) and high mass loadings (180.1 μg$_{Cu}$ cm^{-2}, **Cu_2O_{NPF}(180)**) and performed chronopotentiometry in 1 M $KHCO_3$ (with electrolyte recycling) at current densities between 100-300 mA cm^{-2}. A **CuO_{NPF}(196)** electrode (~196.2 μg cm^{-2}) was also included for comparison. These electrodes appear as batches 10-12 of Table S1.

Figure 5a shows that at 300 mA cm^{-2}, **Cu_2O_{NPF}(20)** reached a maximum methane partial current density of 143 mA cm^{-2} and cathodic energy efficiency towards methane of 20%

Unfortunately, that electrode performance was short-lived because of salt precipitation and Cu dissolution (see Figure S9), in line with previous reports on methane-evolving electrodes.[50-51] After applying a washing step with ultrapure water, the catalytic activity of the electrode recovered partially, allowing the determination of its ECSA. Compared to **Cu$_2$O$_{NPF}$(180)** and **CuO$_{NPF}$(196), Cu$_2$O$_{NPF}$(20)** had the highest C_{DL} and RF (77.4) and accordingly, the lowest degree of GDE coverage (see Figures S10-S11), as discussed before.

In contrast, the **CuO$_{NPF}$(196)** and **Cu$_2$O$_{NPF}$(180)** electrodes suppressed methane evolution almost entirely (< 0.5 and < 2 mA cm^{-2}, respectively) under the same conditions (Figure 5b-c). C_{2+} selectivities and partial current densities peaked at 76.9% (of which 55% to ethylene) and 230.9 mA cm^{-2} for **Cu$_2$O$_{NPF}$(180)** at -1.15V$_{RHE}$, with similar performance for **CuO$_{NPF}$(196).** By one measure, **CuO$_{NPF}$(196)** can be regarded as the superior electrode since it suppresses the evolution of methane to negligible extents. Nevertheless, in terms of the cathodic energy efficiency towards ethylene, both electrodes perform at 26.7 ± 0.5%. Judging by the obtained cathodic energy efficiency and high partial current densities, these electrodes perform very well compared with the literature on conventionally sputtered electrodes and other selected materials in 1M $KHCO_3$ electrolytes[7, 46-49, 52-54] (Table S6-S7).

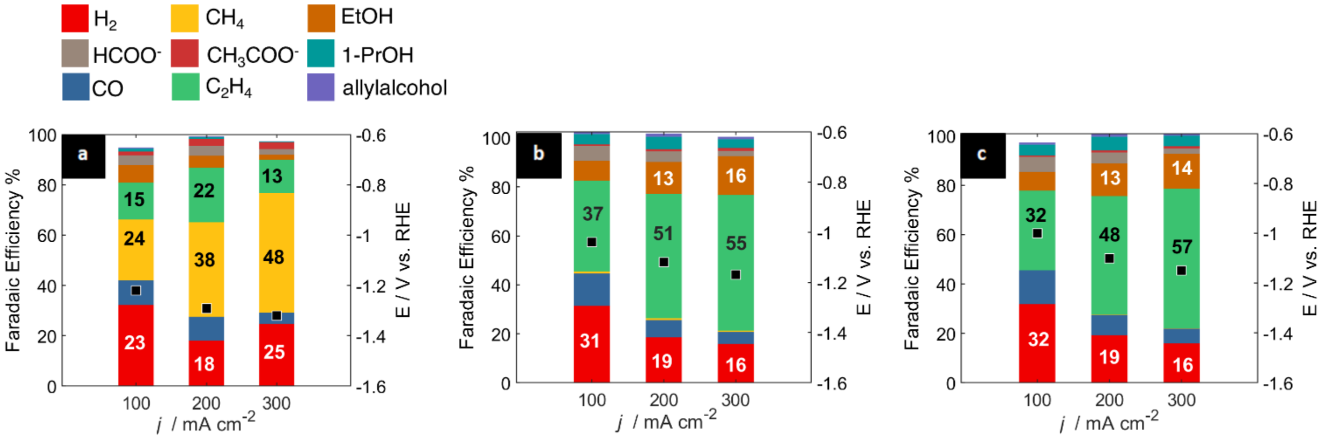

Figure 5 *Selectivity and working electrode potentials of (a)* ***Cu$_2$O$_{NPF}$(20)****, (b)* ***Cu$_2$O$_{NPF}$(180)*** *and (c)* ***CuO$_{NPF}$(196)*** *in 1 M $KHCO_3$ (Initial pH 8.1) at 100-300 mA cm^{-2}. Conditions: Charge passed: 283-353 C, CO_2 flow rate 5-7 sccm, electrolyte flow rate: 0.25 cm^3 cm^{-2} min. Working electrode area 0.785 cm^2. Ohmic resistance ~4 Ω cm^2. The catholyte (4-5 cm^3) was recycled throughout the measurement. Example CP graphs are provided in the supporting information, Figure S8.*

Prospects of SGAS-fabricated Catalyst Layers for CO_2RR Upscaling

In view of these results, we highlight the fact that SGAS-fabricated CuO_x NP films, unlike conventionally sputtered films,[55] are composed initially of individual NPs irrespective of the deposition time. SGAS-fabricated NPs soft-landed already formed onto the substrate,[56] whereas conventional sputtering leads to the formation of a continuous film with increasing deposition time. In other words, using SGAS results in nanoparticulate films that are particularly suited for electrocatalytic applications, where high surface areas and mass-based activity are desired. An example is the performance of **Cu_2O_{NPF}(18)** and **Cu_2O_{NPF}(20)** that registered maximum CH_4 current densities of 114 and 143 mA cm^{-2} in 1 M $KHCO_3$. Those current densities correspond with short-term mass-normalized activities of 6.4 and 7.2 kA/g_{Cu}, which is an improvement of 4-10-fold compared to the state-of-the-art.[50-52] In those literature cases, conventional GDEs are often replaced by dedicated reaction interfaces built around a porous polytetrafluoroethylene (PTFE) membrane[4, 22, 57] to improve hydrophobicity and prolong operation. Here, we used commercially available GDEs, consisting of a ~300 µm-thick network of PTFE-treated carbon fibers, which are covered by a rough ~50 µm-thick hydrophobic microporous layer, the actual substrate for soft-landing. That microporous layer has a high surface area that can accommodate many more NPs as compared to a fiber structure of similar geometric planar dimensions. A related advantage of SGAS fabrication is that it allows one to maintain the substrate's roughness to a greater extent than with conventional sputtering. In the case of the latter, re-sputtering of the ions in the asperities of the substrate causes more ions to enter at angles non-perpendicular to the surface and, thus, lead to the loss of substrate edges, which account for a large share of the substrate's surface area.[58] This, in turn, can affect the wettability of the modified SGAS-fabricated electrodes. To study this effect, water contact-angle measurements were carried out. Figure S12a shows that at low NP loadings (<10 µg cm^{-2}) the surface is nearly super-hydrophobic (θ =144.4°), preserving the hydrophobicity of the underlying GDE ($\theta = 144°$).[59] When sputtering time is increased and more NPs soft-land on top of each other and agglomerate to form a three-dimensional film, the surface becomes hydrophilic ($\theta = 46.1°$, Figure S12b), primarily because of the change in chemical properties of the surface (Cu NP film vs. Cu NP-decorated PTFE-treated carbon). Increasing the loading results in an additional decrease in contact angle to values close to super-hydrophilicity ($\theta = 12.7°$, Figure S12c). In comparison, gas diffusion electrodes that were conventionally sputtered (CS) with Cu are, both in terms of visual appearance and contact angle, more homogeneous (Figures S12d-f).

One could ostensibly explain the difference in contact angle between SGAS-fabricated films and CS-films based on the large differences in their growth mechanism[60] and surface morphology. Lower apparent contact angles for SGAS may be explained by the fact that the ratio of solid-liquid interfacial area to the projected interfacial area increases. If the water droplet is assumed to penetrate the roughness asperities of the SGAS-fabricated films,[61] it becomes plausible that a larger interfacial area brought about by the porosity of the NP film, would lower the apparent contact angle.

Yet despite having a significantly lower contact angle, the highest loading SGAS electrode outlasts its conventionally sputtered counterpart in terms of CO2RR stability and selectivity. Figure 6a shows that the former maintains ethylene FEs of about 50% for 4 hours and total hydrocarbon selectivity >45% for 6 hours under galvanostatic control at 250 mA cm^{-2} in a 1M $KHCO_3$ electrolyte (pH 8.8). Moreover, Figure 6b shows that the ethylene-to-methane ratio of the SGAS-fabricated electrode quintuples that of the CS electrode after 15 minutes of reaction, after which it decays linearly for 3 hours before reaching the initial value of the benchmark. After that point, the rate of decay is similar for both materials, indicating that the degradation mechanism (Cu dissolution, salt precipitation, as discussed before) is similar for both. The stability of both SGAS-fabricated and CS electrodes diminishes with loading (Figure 6c-e), proportional to the initial C_2H_4/CH_4 ratio depicted in Figure 6b. Thus, at high Cu loadings, that ratio appears to be a better predictor of electrode longevity than the measured contact angle of the pre-catalysts. Yet at very low loadings, the latter does show that the hydrophobic properties of the substrate are better preserved with SGAS fabrication. This may prove relevant in future CO_2RR research and catalysis, if the catalytic activity or morphological properties of the support would be of any importance (such as in tandem catalysis concepts).

In this paper, we explored the application of a well-known Cu catalytic system. MICS can of course be applied to form more complex physical/catalytic systems such as alloyed or core@shell bimetallic NPs.[25, 62-63] Yet even in the apparently simple case of Cu NPs, SGAS-fabricated NP films already show several advantages also when compared to wet chemical methods, in particular with respect to material preparation (absence of

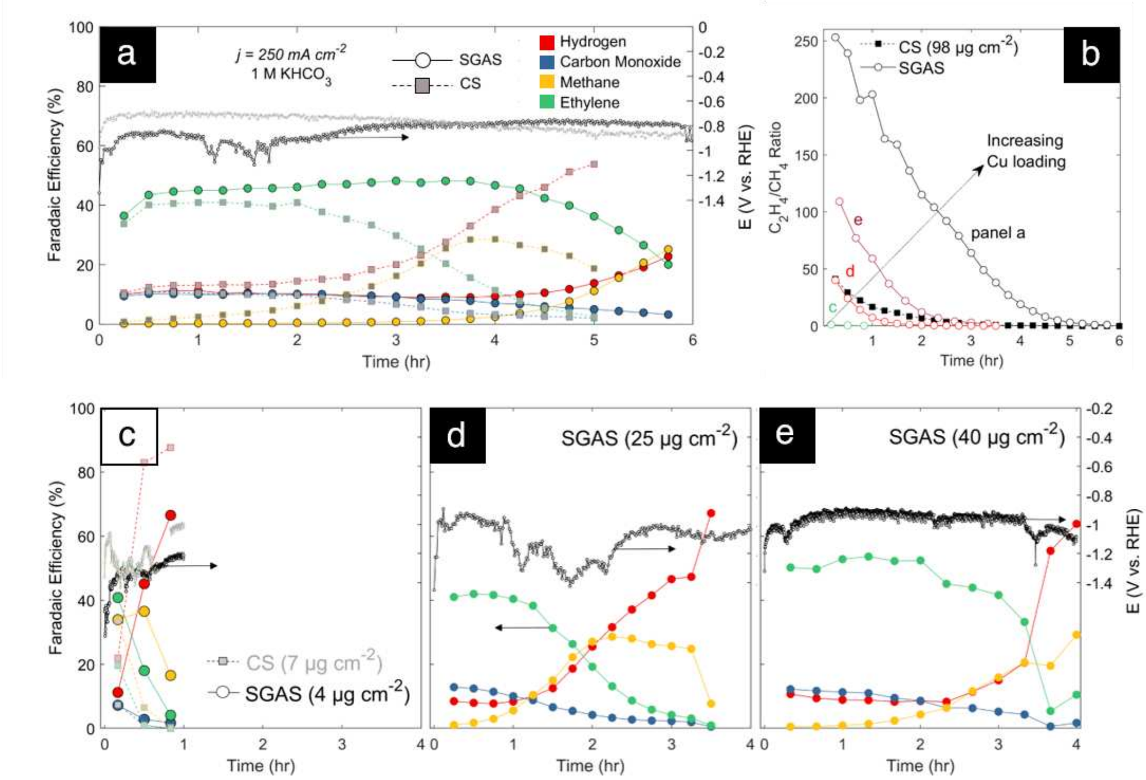

Figure 6 *(a) Comparison of time-dependent selectivity between SGAS-fabricated (Cu_2O_{NPF}, source conditions; batches 7-9 Table S1) and conventionally sputtered (CS) benchmark film/GDEs with loadings of 60 and 98 μg_{Cu} cm^{-2}, respectively (b) Time-dependent C_2H_4/CH_4 ratios for SGAS-fabricated electrodes of increasing loading (4-60 μg cm^{-2}) and comparison with CS-electrode (98 μg cm^{-2}). (c-e) time-dependent gas-phase selectivity of SGAS-fabricated electrodes with increasing loading. Corresponding liquid phase selectivities are given in Figure S13. Tabulated values in Tables S8-S9. Experimental conditions: j_{geo} = 250 mA cm^{-2}, A=0.785 cm^2, $F_{CO2,IN}$ = 7.5 sccm CO_2, F_{CATH} = 0.2 ml/min 1M $KHCO_3$ (single-pass).*

ligands/binder/impurities), handling (absence of toxic byproducts) and deposition (loss of valuable/expensive NPs upon, for example, airbrushing).

Combining all of the above, we therefore argue that SGAS-fabricated NP films could play an important role in advancing future fundamental and applied CO_2RR research aiming at: (a) disentangling the nexus of NP catalytic performance - NP/electrode preparation – processing/reactor conditions and (b) optimizing/upscaling electrolyzer stacks employing NP-based catalyst layers, where a high degree of reproducibility, cleanliness and homogeneity are required to achieve stable operation across multiple cells.

CONCLUSIONS

In this study, we explored the use of a gas aggregation source (MICS type) in producing CuO_x nanoparticle films as CO_2 reduction catalyst layers. It was shown that, depending on the mass loading, CuO_x films could take on different morphologies: (a) evenly dispersed NPs atop a GDE, (b) porous, or (c) compact three-dimensional films made of CuO_x building blocks. We found, using quasi *in situ* XPS, that the films reduce almost entirely to metallic Cu at $-0.85V_{RHE}$, irrespective of their morphology or oxidation state. As a result, evenly dispersed NPs operate at higher overpotentials and yield methane as major product while porous and rough CuO_x NP films yield ethylene and ethanol as major products, as observed from both H-type cell and gas-fed flow-cell experiments. Under commercially relevant conditions, evenly dispersed NP films with a loading of ~20 µg cm^{-2} yield methane as major product (38-48%), while achieving current densities of 113-143 mA cm^{-2} for short electrolysis periods (mass-based activity of up to 7.2 kA/g). CuO_x films with maximum mass loadings of ~200 µg cm^{-2} produce ethylene as major product (55-57%) and reach partial C_{2+} current densities of 230.9 mA cm^{-2} (76%), suppressing methane production almost completely. That versatility, along with the high degree of control over mass loading, oxidation state and high purity composition made possible by MICS, could help future studies aiming at optimizing catalyst layers for CO_2 reduction and a variety of other electrocatalytic reactions.

ASSOCIATED CONTENT

Supporting Information. llustration of the STARDUST machine (Figure S1); Summary of the experimental conditions for the fabrication of CuO_X NPs (Table S1); SEM-EDX investigation of CuO_x deposits on GDEs (S2); LSVs of Cu_2O_{NPF} as a function of deposition time (S3); Additional *ex situ* and *quasi in situ* Cu LMM/Cu 2p spectra and their deconvolution (S4); Summary of LCF analysis (Table S2); Electrochemical performance H-type cell (Table S3); Double layer capacitance measurements (S5); Electrochemical performance flow-cell in 0.1M $KHCO_3$ (Table S4); AFM images of Cu_2O with different particle size (S6); CO2RR selectivity of Cu_2O_{NPF} electrodes with different particle size (S7); CO_2RR performance of Cu_2O_{NPF} electrodes with low mass loadings 1M $KHCO_3$ (Table S5); CO_2RR performance in 1M $KHCO_3$ (Table S6); Comparison with literature (Table S7). (PDF)

AUTHOR INFORMATION

Corresponding Authors

*Nick Daems Nick.Daems@uantwerpen.be

*Tom Breugelmans Tom.Breugelmans@uantwerpen.be

Author contribution

N. Daems – synthesis, conceptualization, project coordination, writing – review & editing; D. Choukroun – SEM, flow cell design and fabrication, electrochemical measurements (flow cell), writing - original draft preparation; P. Merino, G. Santoro, L. Vázquez and L. Martínez – synthesis, ex-situ XPS and AFM analysis, writing – review & editing; C. Rettenmaier and A. Bergmann - in-situ XPS experiments, electrochemical measurements (H-type cell), writing – review & editing; L. Pacquets – electrochemical measurements (flow cell); J.A. Martín Gago, B. Roldan Cuenya and T. Breugelmans - supervision, funding acquisition, writing - review & editing. All authors have given approval to the final version of the manuscript. ‡These authors contributed equally.

Funding Sources

ACKNOWLEDGEMENT

The authors would like to thank María Elena Casero Junquera from the department of Analytical Chemistry and Instrumental Analysis at the Universidad Autonoma de Madrid, Sara Bals of the Electron Microscopy for Materials Science (EMAT) and Bart Van der Bruggen of the ProcESS lab at the KU Leuven for providing access to their lab infrastructure. N.D. and L.P. acknowledge sponsoring from the research foundation of Flanders (FWO, grants 12Y3919N and 1S56920N). We thank the European Research Council for funding support under Synergy grant ERC-2013-SyG, G.A. 610256 (NANOCOSMOS). Also, we acknowledge support from the Spanish MINECO through grants MAT2017-85089-c2-1R and support from the FotoArt-CM Project (P2018/NMT 4367) through the Program of R&D activities between research groups in Technologies 2013, co-financed by European Structural Funds. CR, AB and BRC acknowledge funding from the Deutsche Forschungsgemeinschaft (DFG, German

Research Foundation)– project no. 406944504 – SPP 2080 and the European Research Council (ERC-725915, OPERANDOCAT).

ABBREVIATIONS

SGAS, sputter gas aggregation source; MICS – multiple ion cluster source; CS – conventional sputtering; CO2RR – CO_2 reduction reaction.

REFERENCES

1. Bushuyev, O. S.; De Luna, P.; Dinh, C. T.; Tao, L.; Saur, G.; van de Lagemaat, J.; Kelley, S. O.; Sargent, E. H., What Should We Make with CO_2 and How Can We Make It? *Joule* **2018**, *2*, 825-832.
2. Artz, J.; Müller, T. E.; Thenert, K.; Kleinekorte, J.; Meys, R.; Sternberg, A.; Bardow, A.; Leitner, W., Sustainable Conversion of Carbon Dioxide: An Integrated Review of Catalysis and Life Cycle Assessment. *Chem. Rev.* **2018**, *118*, 434-504.
3. De Luna, P.; Hahn, C.; Higgins, D.; Jaffer, S. A.; Jaramillo, T. F.; Sargent, E. H., What Would It Take for Renewably Powered Electrosynthesis to Displace Petrochemical Processes? *Science* **2019**, *364*, eaav3506.
4. Ozden, A.; Li, F.; García de Arquer, F. P.; Rosas-Hernández, A.; Thevenon, A.; Wang, Y.; Hung, S.-F.; Wang, X.; Chen, B.; Li, J.; Wicks, J.; Luo, M.; Wang, Z.; Agapie, T.; Peters, J. C.; Sargent, E. H.; Sinton, D., High-Rate and Efficient Ethylene Electrosynthesis Using a Catalyst/Promoter/Transport Layer. *ACS Energy Lett.* **2020**, 2811-2818.
5. Li, F.; Thevenon, A.; Rosas-Hernández, A.; Wang, Z.; Li, Y.; Gabardo, C. M.; Ozden, A.; Dinh, C. T.; Li, J.; Wang, Y.; Edwards, J. P.; Xu, Y.; McCallum, C.; Tao, L.; Liang, Z.-Q.; Luo, M.; Wang, X.; Li, H.; O'Brien, C. P.; Tan, C.-S.; Nam, D.-H.; Quintero-Bermudez, R.; Zhuang, T.-T.; Li, Y. C.; Han, Z.; Britt, R. D.; Sinton, D.; Agapie, T.; Peters, J. C.; Sargent, E. H., Molecular Tuning of CO_2-to-Ethylene Conversion. *Nature* **2020**, *577*, 509-513.
6. Gabardo, C. M.; O'Brien, C. P.; Edwards, J. P.; McCallum, C.; Xu, Y.; Dinh, C.-T.; Li, J.; Sargent, E. H.; Sinton, D., Continuous Carbon Dioxide Electroreduction to Concentrated Multi-Carbon Products Using a Membrane Electrode Assembly. *Joule* **2019**, *3*, 2777-2791.
7. Xu, Y.; Li, F.; Xu, A.; Edwards, J. P.; Hung, S.-F.; Gabardo, C. M.; O'Brien, C. P.; Liu, S.; Wang, X.; Li, Y.; Wicks, J.; Miao, R. K.; Liu, Y.; Li, J.; Huang, J. E.; Abed, J.; Wang, Y.; Sargent, E. H.; Sinton, D., Low Coordination Number Copper Catalysts for Electrochemical CO_2 Methanation in a Membrane Electrode Assembly. *Nat. Commun.* **2021**, *12*, 2932.
8. Reske, R.; Mistry, H.; Behafarid, F.; Roldan Cuenya, B.; Strasser, P., Particle Size Effects in the Catalytic Electroreduction of CO_2 on Cu Nanoparticles. *J. Am. Chem. Soc.* **2014**, *136*, 6978-6986.
9. Möller, T.; Scholten, F.; Thanh, T. N.; Sinev, I.; Timoshenko, J.; Wang, X.; Jovanov, Z.; Gliech, M.; Roldan Cuenya, B.; Varela, A. S.; Strasser, P., Electrocatalytic CO_2 Reduction on CuOx Nanocubes: Tracking the Evolution of Chemical State, Geometric Structure, and Catalytic Selectivity Using Operando Spectroscopy. *Angew. Chem. Int. Ed.* **2020**, *59*, 17974-17983.
10. Gao, Y.; Wu, Q.; Liang, X.; Wang, Z.; Zheng, Z.; Wang, P.; Liu, Y.; Dai, Y.; Whangbo, M. H.; Huang, B., Cu_2O Nanoparticles With Both {100} and {111} Facets for Enhancing the Selectivity and Activity of CO_2 Electroreduction to Ethylene. *Adv. Sci.* **2020**, *7*, 1902820.
11. Grosse, P.; Gao, D.; Scholten, F.; Sinev, I.; Mistry, H.; Roldan Cuenya, B., Dynamic Changes in the Structure, Chemical State and Catalytic Selectivity of Cu Nanocubes during CO_2 Electroreduction: Size and Support effects. *Angew. Chem. Int. Ed.* **2018**, *57*, 6192-6197.

12. De Gregorio, G. L.; Burdyny, T.; Loiudice, A.; Iyengar, P.; Smith, W. A.; Buonsanti, R., Facet-Dependent Selectivity of Cu Catalysts in Electrochemical CO_2 Reduction at Commercially Viable Current Densities. *ACS Catal.* **2020**, *10*, 4854-4862.

13. Jiang, K.; Huang, Y.; Zeng, G.; Toma, F. M.; Goddard III, W. A.; Bell, A. T., Effects of Surface Roughness on the Electrochemical Reduction of CO_2 over Cu. *ACS Energy Lett.* **2020**, *5*, 1206-1214.

14. Mistry, H.; Behafarid, F.; Reske, R.; Varela, A. S.; Strasser, P.; Roldan Cuenya, B., Tuning Catalytic Selectivity at the Mesoscale *via* Interparticle Interactions. *ACS Catal.* **2016**, *6*, 1075-1080.

15. Kim, D.; Kley, C. S.; Li, Y.; Yang, P., Copper Nanoparticle Ensembles for Selective Electroreduction of CO_2 to C_2–C_3 Products. *Proc. Natl. Acad. Sci. U. S. A.* **2017**, *114*, 10560-10565.

16. Wang, X.; Varela, A. S.; Bergmann, A.; Kühl, S.; Strasser, P., Catalyst Particle Density Controls Hydrocarbon Product Selectivity in CO_2 Electroreduction on CuOx. *ChemSusChem* **2017**, *10*, 4642-4649.

17. Tan, Y. C.; Lee, K. B.; Song, H.; Oh, J., Modulating Local CO_2 Concentration as a General Strategy for Enhancing C−C Coupling in CO_2 Electroreduction. *Joule* **2020**, *4*, 1104-1120.

18. Velasco-Vélez, J.-J.; Jones, T.; Gao, D.; Carbonio, E.; Arrigo, R.; Hsu, C.-J.; Huang, Y.-C.; Dong, C.-L.; Chen, J.-M.; Lee, J.-F.; Strasser, P.; Roldan Cuenya, B.; Schlögl, R.; Knop-Gericke, A.; Chuang, C.-H., The Role of the Copper Oxidation State in the Electrocatalytic Reduction of CO_2 into Valuable Hydrocarbons. *ACS Sustainable Chem. Eng.* **2019**, *7*, 1485-1492.

19. Kas, R.; Kortlever, R.; Milbrat, A.; Koper, M. T. M.; Mul, G.; Baltrusaitis, J., Electrochemical CO_2 Reduction on Cu_2O-derived Copper Nanoparticles: Controlling the Catalytic Selectivity of Hydrocarbons. *Phys. Chem. Chem. Phys.* **2014**, *16*, 12194-12201.

20. Kas, R.; Kortlever, R.; Yılmaz, H.; Koper, M. T. M.; Mul, G., Manipulating the Hydrocarbon Selectivity of Copper Nanoparticles in CO_2 Electroreduction by Process Conditions. *ChemElectroChem* **2015**, *2*, 354-358.

21. Arán-Ais, R. M.; Scholten, F.; Kunze, S.; Rizo, R.; Roldan Cuenya, B., The Role of *in Situ* Generated Morphological Motifs and Cu(I) Species in C_{2+} Product Selectivity during CO_2 Pulsed Electroreduction. *Nat. Energy* **2020**, *5*, 317-325.

22. Dinh, C.-T.; Burdyny, T.; Kibria, M. G.; Seifitokaldani, A.; Gabardo, C. M.; de Arquer, F. P. G.; Kiani, A.; Edwards, J. P.; De Luna, P.; Bushuyev, O. S., CO_2 Electroreduction to Ethylene via Hydroxide-Mediated Copper Catalysis at an Abrupt Interface. *Science* **2018**, *360*, 783-787.

23. Manthiram, K.; Beberwyck, B. J.; Alivisatos, A. P., Enhanced Electrochemical Methanation of Carbon Dioxide with a Dispersible Nanoscale Copper Catalyst. *J. Am. Chem. Soc.* **2014**, *136*, 13319-13325.

24. De Arquer, F. P. G.; Dinh, C.-T.; Ozden, A.; Wicks, J.; McCallum, C.; Kirmani, A. R.; Nam, D.-H.; Gabardo, C.; Seifitokaldani, A.; Wang, X., CO_2 Electrolysis to Multicarbon Products at Activities Greater than 1 A cm^{-2}. *Science* **2020**, *367*, 661-666.

25. Llamosa, D.; Ruano, M.; Martínez, L.; Mayoral, A.; Roman, E.; García-Hernández, M.; Huttel, Y., The Ultimate Step Towards a Tailored Engineering of Core@Shell and Core@Shell@Shell Nanoparticles. *Nanoscale* **2014**, *6*, 13483-13486.

26. Martínez, L.; Lauwaet, K.; Santoro, G.; Sobrado, J. M.; Peláez, R. J.; Herrero, V. J.; Tanarro, I.; Ellis, G. J.; Cernicharo, J.; Joblin, C.; Huttel, Y.; Martín-Gago, J. A., Precisely Controlled Fabrication, Manipulation and *in-Situ* Analysis of Cu Based Nanoparticles. *Sci. Rep.* **2018**, *8*, 7250.

27. Spadaro, M. C.; Humphrey, J. J. L.; Cai, R.; Martínez, L.; Haigh, S. J.; Huttel, Y.; Spencer, S. J.; Wain, A. J.; Palmer, R., Electrocatalytic Behavior of PtCu Clusters Produced by Nanoparticle Beam Deposition. *J. Phys. Chem. C* **2020**, *124*, 23683-23689.

28. Palmer, R. E.; Cai, R.; Vernieres, J., Synthesis Without Solvents: The Cluster (Nanoparticle) Beam Route to Catalysts and Sensors. *Acc. Chem. Res.* **2018**, *51*, 2296-2304.

29. Martínez, L.; Santoro, G.; Merino, P.; Accolla, M.; Lauwaet, K.; Sobrado, J.; Sabbah, H.; Pelaez, R. J.; Herrero, V. J.; Tanarro, I.; Agúndez, M.; Martín-Jimenez, A.; Otero, R.; Ellis, G. J.; Joblin, C.; Cernicharo, J.; Martín-Gago, J. A., Prevalence of Non-Aromatic Carbonaceous Molecules in the Inner Regions of Circumstellar Envelopes. *Nat. Astron.* **2020**, *4*, 97-105.

30. Díaz, M.; Martínez, L.; Ruano, M. M.; Llamosa P, D.; Román, E.; García-Hernandez, M.; Ballesteros, C.; Fermento, R.; Cebollada, A.; Armelles, G.; Huttel, Y., Morphological, Structural, and Magnetic Properties of Co Nanoparticles in a Silicon Oxide Matrix. *J. Nanoparticle Res.* **2011**, *13*, 5321.

31. Horcas, I.; Fernández, R.; Gómez-Rodríguez, J. M.; Colchero, J.; Gómez-Herrero, J.; Baro, A. M., WSXM: A Software for Scanning Probe Microscopy and a Tool for Nanotechnology. *Review of Scientific Instruments* **2007**, *78*, 013705.

32. Le, M.; Ren, M.; Zhang, Z.; Sprunger, P. T.; Kurtz, R. L.; Flake, J. C., Electrochemical Reduction of CO_2 to CH_3OH at Copper Oxide Surfaces. *Journal of The Electrochemical Society* **2011**, *158*, E45-E49.

33. Arán-Ais, R. M.; Scholten, F.; Kunze, S.; Rizo, R.; Roldan Cuenya, B., The role of in situ generated morphological motifs and Cu(i) species in C2+ product selectivity during CO2 pulsed electroreduction. *Nature Energy* **2020**.

34. Velasco-Vélez, J.-J.; Chuang, C.-H.; Gao, D.; Zhu, Q.; Ivanov, D.; Jeon, H. S.; Arrigo, R.; Mom, R. V.; Stotz, E.; Wu, H.-L.; Jones, T. E.; Roldan Cuenya, B.; Knop-Gericke, A.; Schlögl, R., On the Activity/Selectivity and Phase Stability of Thermally Grown Copper Oxides during the Electrocatalytic Reduction of CO_2. *ACS Catal.* **2020**, *10*, 11510-11518.

35. Li, Y.; Xu, A.; Lum, Y.; Wang, X.; Hung, S.-F.; Chen, B.; Wang, Z.; Xu, Y.; Li, F.; Abed, J.; Huang, J. E.; Rasouli, A. S.; Wicks, J.; Sagar, L. K.; Peng, T.; Ip, A. H.; Sinton, D.; Jiang, H.; Li, C.; Sargent, E. H., Promoting CO_2 Methanation via Ligand-Stabilized Metal Oxide Clusters as Hydrogen-Donating Motifs. *Nat. Commun.* **2020**, *11*, 6190.

36. Kuhl, K. P.; Cave, E. R.; Abram, D. N.; Jaramillo, T. F., New Insights into the Electrochemical Reduction of Carbon Dioxide on Metallic Copper Surfaces. *Energy Environ. Sci.* **2012**, *5*, 7050-7059.

37. Hori, Y.; Murata, A.; Takahashi, R., Formation of Hydrocarbons in the Electrochemical Reduction of Carbon Dioxide at a Copper Electrode in Aqueous Solution. *Journal of the Chemical Society, Faraday Transactions 1: Physical Chemistry in Condensed Phases* **1989**, *85*, 2309-2326.

38. Singh, M. R.; Kwon, Y.; Lum, Y.; Ager, J. W.; Bell, A. T., Hydrolysis of Electrolyte Cations Enhances the Electrochemical Reduction of CO_2 over Ag and Cu. *J. Am. Chem. Soc.* **2016**, *138*, 13006-13012.

39. Varela, A. S.; Kroschel, M.; Reier, T.; Strasser, P., Controlling the Selectivity of CO_2 Electroreduction on Copper: The Effect of the Electrolyte Concentration and The Importance of The Local pH. *Catal. Today* **2016**, *260*, 8-13.

40. Gupta, N.; Gattrell, M.; MacDougall, B., Calculation for the Cathode Surface Concentrations in the Electrochemical Reduction of CO_2 in $KHCO_3$ Solutions. *J. Appl. Electrochem.* **2006**, *36*, 161-172.

41. Singh, M. R.; Clark, E. L.; Bell, A. T., Effects of Electrolyte, Catalyst, and Membrane Composition and Operating Conditions on the Performance of Solar-Driven Electrochemical Reduction of Carbon Dioxide. *Phys. Chem. Chem. Phys.* **2015**, *17*, 18924-18936.

42. Schouten, K. J. P.; Qin, Z.; Gallent, E. P.; Koper, M. T. M., Two Pathways for the Formation of Ethylene in CO Reduction on Single-Crystal Copper Electrodes. *J. Am. Chem. Soc.* **2012**, *134*, 9864-9867.

43. Jeon, H. S.; Timoshenko, J.; Rettenmaier, C.; Herzog, A.; Yoon, A.; Chee, S. W.; Oener, S.; Hejral, U.; Haase, F. T.; Roldan Cuenya, B., Selectivity Control of Cu Nanocrystals in a Gas-Fed Flow Cell through CO_2 Pulsed Electroreduction. *J. Am. Chem. Soc.* **2021**, *143*, 7578-7587.

44. Higgins, D.; Hahn, C.; Xiang, C.; Jaramillo, T. F.; Weber, A. Z., Gas-Diffusion Electrodes for Carbon Dioxide Reduction: A New Paradigm. *ACS Energy Lett.* **2019**, *4*, 317-324.

45. Burdyny, T.; Smith, W. A., CO_2 Reduction on Gas-Diffusion Electrodes and Why Catalytic Performance Must be Assessed at Commercially-Relevant Conditions. *Energy Environ. Sci.* **2019**, *12*, 1442-1453.

46. Ma, M.; Clark, E. L.; Therkildsen, K. T.; Dalsgaard, S.; Chorkendorff, I.; Seger, B., Insights into the Carbon Balance for CO_2 Electroreduction on Cu Using Gas Diffusion Electrode Reactor Designs. *Energy Environ. Sci.* **2020**, *13*, 977-985.

47. Zhang, J.; Luo, W.; Züttel, A., Crossover of Liquid Products from Electrochemical CO_2 Reduction through Gas Diffusion Electrode and Anion Exchange Membrane. *J. Catal.* **2020**, *385*, 140-145.

48. Li, Y. G. C.; Wang, Z. Y.; Yuan, T. G.; Nam, D. H.; Luo, M. C.; Wicks, J.; Chen, B.; Li, J.; Li, F. W.; de Arguer, F. P. G.; Wang, Y.; Dinh, C. T.; Voznyy, O.; Sinton, D.; Sargent, E. H., Binding Site Diversity Promotes CO_2 Electroreduction to Ethanol. *J. Am. Chem. Soc.* **2019**, *141*, 8584-8591.

49. Wang, Y.; Wang, Z.; Dinh, C.-T.; Li, J.; Ozden, A.; Golam Kibria, M.; Seifitokaldani, A.; Tan, C.-S.; Gabardo, C. M.; Luo, M.; Zhou, H.; Li, F.; Lum, Y.; McCallum, C.; Xu, Y.; Liu, M.; Proppe, A.; Johnston, A.; Todorovic, P.; Zhuang, T.-T.; Sinton, D.; Kelley, S. O.; Sargent, E. H., Catalyst Synthesis under CO_2 Electroreduction Favours Faceting and Promotes Renewable Fuels Electrosynthesis. *Nat. Catal.* **2020**, *3*, 98-106.

50. Zhang, T.; Verma, S.; Kim, S.; Fister, T. T.; Kenis, P. J. A.; Gewirth, A. A., Highly Dispersed, Single-Site Copper Catalysts for the Electroreduction of CO_2 to Methane. *Journal of Electroanalytical Chemistry* **2020**, 113862.

51. Sedighian Rasouli, A.; Wang, X.; Wicks, J.; Lee, G.; Peng, T.; Li, F.; McCallum, C.; Dinh, C.-T.; Ip, A. H.; Sinton, D.; Sargent, E. H., CO_2 Electroreduction to Methane at Production Rates Exceeding 100 mA/cm^2. *ACS Sustainable Chem. Eng.* **2020**, *8*, 14668-14673.

52. Wang, X.; Xu, A.; Li, F.; Hung, S.-F.; Nam, D.-H.; Gabardo, C. M.; Wang, Z.; Xu, Y.; Ozden, A.; Rasouli, A. S.; Ip, A. H.; Sinton, D.; Sargent, E. H., Efficient Methane Electrosynthesis Enabled by Tuning Local CO_2 Availability. *J. Am. Chem. Soc.* **2020**, *142*, 3525-3531.

53. Wang, X.; Ou, P.; Wicks, J.; Xie, Y.; Wang, Y.; Li, J.; Tam, J.; Ren, D.; Howe, J. Y.; Wang, Z.; Ozden, A.; Finfrock, Y. Z.; Xu, Y.; Li, Y.; Rasouli, A. S.; Bertens, K.; Ip, A. H.; Graetzel, M.; Sinton, D.; Sargent, E. H., Gold-in-Copper at Low *CO Coverage Enables Efficient Electromethanation of CO_2. *Nat. Commun.* **2021**, *12*, 3387.

54. Fan, Q.; Zhang, X.; Ge, X.; Bai, L.; He, D.; Qu, Y.; Kong, C.; Bi, J.; Ding, D.; Cao, Y.; Duan, X.; Wang, J.; Yang, J.; Wu, Y., Manipulating Cu Nanoparticle Surface Oxidation States Tunes Catalytic Selectivity toward CH_4 or C_{2+} Products in CO_2 Electroreduction. *Adv. Energy Mater.*, *n/a*, 2101424.

55. Kratochvíl, J.; Kuzminova, A.; Kylián, O.; Biederman, H., Comparison of Magnetron Sputtering and Gas Aggregation Nanoparticle Source Used for Fabrication of Silver Nanoparticle Films. *Surface and Coatings Technology* **2015**, *275*, 296-302.

56. Johnson, G. E.; Colby, R.; Laskin, J., Soft Landing of Bare Nanoparticles with Controlled Size, Composition, and Morphology. *Nanoscale* **2015**, *7*, 3491-3503.

57. Dinh, C.-T.; García de Arquer, F. P.; Sinton, D.; Sargent, E. H., High Rate, Selective, and Stable Electroreduction of CO_2 to CO in Basic and Neutral Media. *ACS Energy Lett.* **2018**, *3*, 2835-2840.

58. Macak, E. B.; Münz, W.-D.; Rodenburg, J. M., Plasma–Surface Interaction at Sharp Edges and Corners During Ion-Assisted Physical Vapor Deposition. Part I: Edge-Related Effects and Their Influence on Coating Morphology and Composition. *J. Appl. Phys.* **2003**, *94*, 2829-2836.

59. Endrődi, B.; Samu, A.; Kecsenovity, E.; Halmágyi, T.; Sebők, D.; Janáky, C., Operando Cathode Activation with Alkali Metal Cations for High Current Density Operation of Water-Fed Zero-Gap Carbon Dioxide Electrolysers. *Nat. Energy* **2021**, *6*, 439-448.

60. Pletea, M.; Brückner, W.; Wendrock, H.; Kaltofen, R., Stress Evolution during and after Sputter Deposition of Cu Thin Films onto Si (100) Substrates under Various Sputtering Pressures. *J. Appl. Phys.* **2005**, *97*, 054908.

61. Zahiri, B.; Sow, P. K.; Kung, C. H.; Mérida, W., Understanding the Wettability of Rough Surfaces using Simultaneous Optical and Electrochemical Analysis of Sessile Droplets. *J. Colloid Interface Sci.* **2017**, *501*, 34-44.

62. Soler-Morala, J.; Jefremovas, E. M.; Martínez, L.; Mayoral, Á.; Sánchez, E. H.; De Toro, J. A.; Navarro, E.; Huttel, Y., Spontaneous Formation of Core@shell Co@Cr Nanoparticles by Gas Phase Synthesis. *Applied Nano* **2020**, *1*, 87-101.

63. Yin, F.; Wang, Z. W.; Palmer, R. E., Controlled Formation of Mass-Selected Cu–Au Core–Shell Cluster Beams. *J. Am. Chem. Soc.* **2011**, *133*, 10325-10327.

TOC Graphic

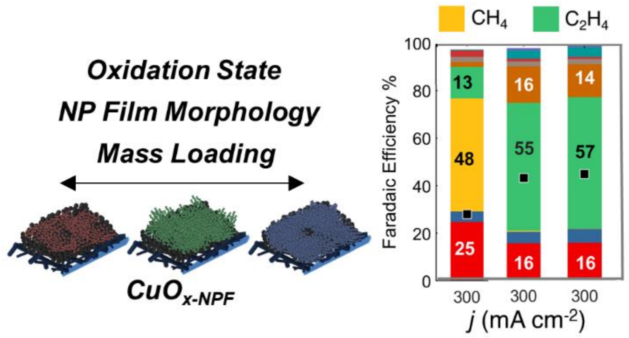
Oxidation State
NP Film Morphology
Mass Loading
CuO$_{x\text{-}NPF}$
CH$_4$
C$_2$H$_4$
Faradaic Efficiency %
100
80
60
40
20
0
13
48
25
16
55
16
14
57
16
300
300
300
j (mA cm^{-2})